The 9th European Congress on Computational Methods in Applied Sciences and Engineering
ECCOMAS Congress 2024
3–7 June 2024, Lisboa, Portugal

SIMULATION OF TRI-AXIAL STRESS REDISTRIBUTION EFFECT IN CONCRETE UNDER FATIGUE LOADING: LATTICE DISCRETE MODEL VS. MICROPLANE MODEL

M. Aguilar[1], A. Baktheer[1], R. Wan-Wendner[2], J. Vorel[3], M. Vořechovský[4] and R. Chudoba[1]

[1] Institute of Structural Concrete, RWTH Aachen University,
Mies-van-der-Rohe-Straße 1, 52074 Aachen, Germany

[2] Department of Structural Engineering and Building Materials, Ghent University,
Technologiepark-Zwijnaarde 60, Gent, 9052, Belgium

[3] Department of Mechanics, Faculty of Civil Engineering, Czech Technical University in Prague,
Thákurova 7, 166 29 Praha 6, Czech Republic

[4] Institute of Structural Mechanics, Brno University of Technology,
Veveří 95, 602 00 Brno, Czech Republic

Key words: Fatigue, Cyclic loading, Fracture, Damage, Microplane theory, Lattice discrete modeling

Summary.

This work aims to develop advanced macro- and mesoscale numerical models to accurately reflect the mechanisms behind the initiation and propagation of concrete fatigue damage. A thermodynamically formulated generalized interface model, that relates fatigue damage growth to cumulative inter-aggregate sliding deformations, is used to describe the interface behavior under monotonic and subcritical cyclic loading. This model is applied to two concrete material structure idealizations: the lattice discrete particle model (LDPM) and the microplane model. The mesoscale lattice discrete particle model explicitly reflects interactions between aggregates and local stress redistribution during fatigue. It is compared to the microplane fatigue model MS1 in combination with finite elements (FE), a semi-multiscale model that can capture the anisotropic nature of concrete while remaining at the macroscopic level. Both approaches, based on the same fatigue damage hypothesis, are evaluated for their ability to reproduce fatigue phenomena such as the evolution of fatigue creep curves and the changing shape of hysteretic loops.

1 INTRODUCTION

Resistance to cyclic loading is crucial for the efficient and reliable design of concrete structures such as roads, rail bridges, and wind turbine towers. Particularly, in wind turbine towers compressive concrete fatigue is of key importance [1, 2, 3]. Understanding concrete fatigue behavior can reduce material consumption, extend service life, and improve structural reliability.

The objective of this study is to investigate the phenomenon of compression fatigue in concrete and its associated stress redistribution. In order to do so, we use two approaches for reproducing concrete

fatigue. The first approach is based on standard continuum mechanics, following the ideas of classical phenomenological tensorial models within the framework of damage-plasticity[4, 5, 6]. These models are computationally efficient and can effectively reproduce the macroscopically observable responses of concrete fatigue, such as the prediction of Wöhler (S-N) curves and fatigue creep curves [7]. As recognized in tensile fatigue loading [8], tri-axial stress redistribution is a critical feature for realistic fatigue modeling under compression. This feature was incorporated into the microplane model MS1 [9], which is used in the present work in combination with finite elements (FE) [10]. The second approach consists of a mesoscale model featuring discrete representations of the concrete material structure [11, 12], following the framework proposed in [13]. Using a discrete model allows for the reproduction of fatigue-induced changes in the material structure, such as crack evolution and aggregate interlock, including the aforementioned tri-axial stress redistribution [14]. Additionally, these mesoscale models implicitly consider the random nature of the spatial distribution of aggregates [15]. The objective of this work is to contribute to the development of advanced macro- and mesoscopic numerical models that can realistically cover the mechanisms governing the initiation and propagation of concrete fatigue damage.

2 THERMODYNAMIC FORMULATION

In order to model concrete fatigue, the authors have developed a thermodynamically based constitutive framework, which is presented in detail in [16]. By making use of this framework, the authors have been able to derive the formulation of an interface model that can be embedded on a generic microplane within a microplane model or at the level of inter-aggregate contact on a lattice discrete particle model. This framework is based on the hypothesis positing that fatigue damage evolution in concrete is primarily related to inter-aggregate cumulative inelastic shear strain [17, 16]. This hypothesis has proven valuable in modeling the fatigue behavior of cementitious interfaces and concrete under compressive fatigue loading in cylinders [9, 18, 19].

2.1 Free energy potential, state variables and thermodynamic forces

The relative displacement of two points connected via the interface is represented by a normal (out-of-plane) component $u_{\mathrm{N}} \equiv u_z$ and an (in-plane) sliding vector $\boldsymbol{u}_{\mathrm{T}} = \{u_x, u_y\}^{\mathsf{T}}$. The vector of kinematic variables defining the irreversible state of the interface is introduced as follows

$$\mathcal{E} := \left[u_{\mathrm{N}}^{\mathrm{p}},\ \omega_{\mathrm{N}}, \boldsymbol{u}_{\mathrm{T}}^{\mathrm{p}},\ \omega_{\mathrm{T}},\ z,\ \boldsymbol{\alpha}\right]. \tag{1}$$

To provide a transparent representation of dissipative mechanisms in the normal and tangential directions, the free energy is introduced as a sum of out-of-plane opening (N) and in-plane sliding (T) contributions

$$\rho\psi(\mathcal{E}) := \rho\psi_{\mathrm{N}}(\mathcal{E}) + \rho\psi_{\mathrm{T}}(\mathcal{E}). \tag{2}$$

Free energy associated with interface opening and closing (N) is defined as a function of total displacement u_{N}, plastic displacement $u_{\mathrm{N}}^{\mathrm{p}}$, and damage ω_{N} as

$$\rho\psi_{\mathrm{N}}(u_{\mathrm{N}}, u_{\mathrm{N}}^{\mathrm{p}}, \omega_{\mathrm{N}}) := \frac{1}{2}\left(1 - H(\sigma_{\mathrm{N}})\,\omega_{\mathrm{N}}\right) E_{\mathrm{N}}(u_{\mathrm{N}} - u_{\mathrm{N}}^{\mathrm{p}})^2, \tag{3}$$

where E_{N} denotes the stiffness. The Heaviside step function $H(.)$ is used to introduce the unilateral effect by activating the damage only for positive values of the traction stress σ_{N}. The free energy associated

with the interface sliding is defined as a function of total sliding vector $\boldsymbol{u}_{\mathrm{T}}$, plastic sliding vector $\boldsymbol{u}_{\mathrm{T}}^{\mathrm{p}}$, tangential damage ω_{T}, and the displacement variables corresponding to isotropic and kinematic hardening, z and $\boldsymbol{\alpha} = [\alpha_x, \alpha_y]$, respectively, as

$$\rho\psi_{\mathrm{T}}(\boldsymbol{u}_{\mathrm{T}}, \boldsymbol{u}_{\mathrm{T}}^{\mathrm{p}}, \omega_{\mathrm{T}}, z, \boldsymbol{\alpha}) := \frac{1}{2}(1-\omega_{\mathrm{T}})E_{\mathrm{T}}\left[(\boldsymbol{u}_{\mathrm{T}} - \boldsymbol{u}_{\mathrm{T}}^{\mathrm{p}})^{\mathsf{T}} \cdot (\boldsymbol{u}_{\mathrm{T}} - \boldsymbol{u}_{\mathrm{T}}^{\mathrm{p}})\right] + \frac{1}{2}Kz^2 + \frac{1}{2}\gamma(\boldsymbol{\alpha}^{\mathsf{T}} \cdot \boldsymbol{\alpha}), \tag{4}$$

where E_{T} denotes the tangential stiffness, K the isotropic and γ the kinematic hardening moduli. The thermodynamic forces are obtained by differentiating the free energy with respect to the kinematic state variables

$$\mathcal{S} = \boldsymbol{\Upsilon}\,\frac{\partial\rho\psi(\mathcal{E})}{\partial\mathcal{E}}. \tag{5}$$

The sign vector operator $\boldsymbol{\Upsilon}$ is introduced to render positive thermodynamic force for positive state variable. To distinguish the thermodynamic forces based on the in correspondence with the definition of the state vector in Eq. (1), let us introduce the generalized vector of thermodynamic forces as

$$\mathcal{S} := \left[\sigma_{\mathrm{N}}^{\mathrm{p}},\, Y_{\mathrm{N}},\, \boldsymbol{\sigma}_{\mathrm{T}}^{\mathrm{p}},\, Y_{\mathrm{T}},\, Z,\, \boldsymbol{X}\right]. \tag{6}$$

The individual components of this vector can be obtained using Eq. (5) The individual components of this vector are obtained using Eq. (5). The normal plastic stress $\sigma_{\mathrm{N}}^{\mathrm{p}}$ and normal energy release rate Y_{N} read

$$\sigma_{\mathrm{N}}^{\mathrm{p}} = -\rho\frac{\partial\psi(\mathcal{E})}{\partial u_{\mathrm{N}}^{\mathrm{p}}} = \left(1 - H(\sigma_{\mathrm{N}}^{\mathrm{p}})\,\omega_{\mathrm{N}}\right)E_{\mathrm{N}}(u_{\mathrm{N}} - u_{\mathrm{N}}^{\mathrm{p}}), \tag{7}$$

$$Y_{\mathrm{N}} = -\rho\frac{\partial\psi(\mathcal{E})}{\partial\omega_{\mathrm{N}}} = \frac{1}{2}E_{\mathrm{N}}(u_{\mathrm{N}} - u_{\mathrm{N}}^{\mathrm{p}})^2. \tag{8}$$

As discussed above, the Heaviside switches off the damage in compression to represent the stiffness recovery upon interface closure. The tangential plastic stress vector $\boldsymbol{\sigma}_{\mathrm{T}}^{\mathrm{p}}$, energy release rate Y_{T}, isotropic hardening stress Z and back stress $\boldsymbol{X} = \{X_x, X_y\}^{\mathsf{T}}$ are obtained as follows

$$\boldsymbol{\sigma}_{\mathrm{T}}^{\mathrm{p}} = -\rho\frac{\partial\psi(\mathcal{E})}{\partial\boldsymbol{u}_{\mathrm{T}}^{\mathrm{p}}} = (1-\omega_{\mathrm{T}})E_{\mathrm{T}}(\boldsymbol{u}_{\mathrm{T}} - \boldsymbol{u}_{\mathrm{T}}^{\mathrm{p}}) \tag{9}$$

$$Y_{\mathrm{T}} = -\rho\frac{\partial\psi(\mathcal{E})}{\partial\omega_{\mathrm{T}}} = \frac{1}{2}E_{\mathrm{T}}\left[(\boldsymbol{u}_{\mathrm{T}} - \boldsymbol{u}_{\mathrm{T}}^{\mathrm{p}})^{\mathsf{T}} \cdot (\boldsymbol{u}_{\mathrm{T}} - \boldsymbol{u}_{\mathrm{T}}^{\mathrm{p}})\right] \tag{10}$$

$$Z = \rho\frac{\partial\psi(\mathcal{E})}{\partial z} = Kz, \quad \boldsymbol{X} = \rho\frac{\partial\psi(\mathcal{E})}{\partial\boldsymbol{\alpha}} = \gamma\,\boldsymbol{\alpha}. \tag{11}$$

2.2 Elementary study at the interface level

To verify the elementary behavior of an interface included in the LDPM or microplane model, as well as to illustrate the ability to assess the fractions of energy dissipated associated with each specific mechanism, we present a fundamental study of its cyclic behavior for the tangential direction in Fig. 1, considering two scenarios. The first scenario maintained a normal pressure of 0 MPa, while the second scenario involved a prior compression displacement of 0.4 cm, equivalent to 40 MPa. In both cases, the cyclic shear load ranged from 0.25 mm to -0.25 mm and was applied through a cyclic displacement-controlled

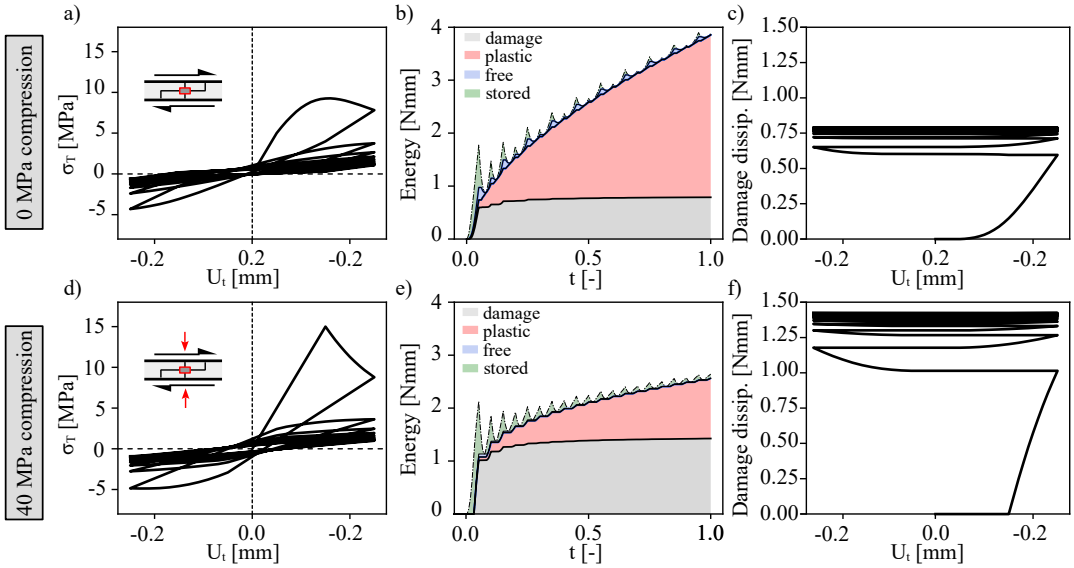

Figure 1: Elementary interface behavior covering the shear behavior. The panels on the left correspond to the stress slip curve, the middle panels show the evolution of energy breakdown, showing the corresponding fractions of energy dissipation due to damage and plasticity and kinematic and stored energy. The panels on the right correspond to the damage evolution with respect to the oscillating displacement loading. Material parameters: E_T = 100, σ_T^0 = 5.0, γ_T = 500, K_T = 0, S_T = 0.02, r_T = 1.0, c_T = 2.0, p_T = 1.0, m_T = 0.25

load. The left panels of Fig. 1 show the resulting stress response. It can be observed that the interface strength increases as the normal compression increases. This is a characteristic aspect of the present formulation, where the tangential strength increases linearly by $m_T\sigma_N$. In this case, the interface has a tangential elastic limit of 5 MPa when compression is not applied. It exhibits a plastic behavior with some hardening afterward, as shown in Figure 1a. On the other hand, the interface that undergoes compression prior to cyclic loading experiences a 10 MPa increase in its elastic limit, displaying a brittle rather than plastic behavior in the post-peak regime, due to a larger value of accumulated elastic energy on the onset of inelasticity, as shown in Fig. 1e. In both cases, there is a significant reduction in stiffness after the first cycle, along with plastic deformation upon passing through the zero stress level.

The two distinct behaviors of the confined and unconfined interfaces are also evident in the energy dissipation breakdown displayed in Fig. 1b and e, which show the numerically quantified stored and dissipated energy at the interface. As shown in Fig. 1b, the interface without compression exhibits more plastic behavior, leading to greater plastic dissipation compared to the interface with prior compression. The interface undergoing compression has a higher shear strength, resulting in the accumulation of more elastic energy. This leads to a faster energy release and greater energy dissipation due to damage during the first cycle, as depicted by the gray area in Fig. 1b and e. The damage and plastic dissipation rates decrease over successive cycles as they are coupled. The green area represents the stored elastic energy which increases during loading and decreases during unloading until it reaches zero every time the stress-slip curve intersects the zero tangential stress axis. During each cycle, the elastic strain available decreases while the maximum tangential stress progressively decreases, leading to a subsequent decrease in the maximum stored elastic energy at the peak of each cycle. Isotropic free energy is visible in light blue, following the same trend as the stored energy.

Fig. 1c and f show the damage energy dissipation as a function of the applied displacement. The model successfully slows down damage accumulation for successive loading cycles, which is an essential feature of models that can realistically capture the fatigue response of concrete.

3 MICROPLANE MODEL

Unlike the classical constitutive models, which establish a direct relation between the strain and stress *tensors*, the microplane models introduce a constitutive relation between strain and stress *vectors* at the level of projected planes, effectively replicating the anisotropic behavior of concrete.

Kinematic constraint: The strain tensor is projected onto each microplane to obtain strain vectors consisting of the normal and tangential components using the so called kinematic constraint

$$\varepsilon_{\mathrm{N}} = \boldsymbol{N} : \boldsymbol{\varepsilon}, \qquad \boldsymbol{\varepsilon}_{\mathrm{T}} = \mathrm{T} : \boldsymbol{\varepsilon}, \tag{12}$$

where the scalar ε_{N} is the normal microplane strain, and $\boldsymbol{\varepsilon}_{\mathrm{T}}$ is the tangential microplane strain vector. The second order normal tensor $\boldsymbol{N}$ and the third order tangential tensor $\boldsymbol{T}$ are given as

$$\boldsymbol{N} = \boldsymbol{n} \otimes \boldsymbol{n}, \qquad \mathrm{T} = \boldsymbol{n} \cdot \mathbb{I}_{sym} - \boldsymbol{n} \otimes \boldsymbol{n} \otimes \boldsymbol{n}, \tag{13}$$

where $\boldsymbol{n}$ is the microplane normal vector and $\mathbb{I}$ is the fourth-order identity tensor.

Constitutive behavior: The constitutive behavior of the proposed microplane model is governed by the thermodynamically based constitutive laws described in Sec. 2 governing the macroscopic behavior. These constitutive laws are defined on the generic microplanes and introduce the dissipative mechanisms for the normal and tangential direction.

Homogenization: The macroscopic stress tensor can be obtained as follows

$$\boldsymbol{\sigma} = \boldsymbol{\beta} : \boldsymbol{C}^{\mathrm{e}} : \boldsymbol{\beta}^{\mathrm{T}} : (\boldsymbol{\varepsilon} - \boldsymbol{\varepsilon}^{\mathrm{p}}), \tag{14}$$

where $\boldsymbol{\beta}$ is the fourth order damage inverse/integrity tensor, $\boldsymbol{C}^{\mathrm{e}}$ is the fourth order elasticity tensor, and $\boldsymbol{\varepsilon}^{\mathrm{p}}$ is the macroscopic plastic strain tensor. According to [20] the macroscopic plastic strain tensor can be obtained by integrating microplane plastic strains as follows

$$\boldsymbol{\varepsilon}^{p}_{ij} = \frac{3}{2\pi} \int_{\Omega} \varepsilon_N^{p,\mathrm{mic}} n_i n_j \, \mathrm{d}\Omega + \frac{3}{2\pi} \int_{\Omega} \frac{\varepsilon_{Tr}^{\pi,\mathrm{mic}}}{2} (n_i \delta_{rj} + n_j \delta_{ri}) \, \mathrm{d}\Omega. \tag{15}$$

The fourth order damage inverse/integrity tensor $\boldsymbol{\beta}$ can be obtained by integrating the normal and tangential microplane damage parameters as follows

$$\begin{aligned} \boldsymbol{\beta}_{ijkl} = & \frac{3}{2\pi} \int_{\Omega} \beta_{\mathrm{N}} \, n_i \, n_j \, n_k \, n_l \, \mathrm{d}\Omega \\ & + \frac{3}{2\pi} \int_{\Omega} \frac{\beta_{\mathrm{T}}}{4} \left(n_i \, n_k \delta_{jl} + n_i \, n_l \delta_{jk} + n_j \, n_k \delta_{il} + n_j \, n_l \delta_{ik} - 4 n_i \, n_j \, n_k \, n_l \right) \, \mathrm{d}\Omega \end{aligned} \tag{16}$$

where $\beta_{\mathrm{N}}^{\mathrm{mic}} = \sqrt{1 - \omega_{\mathrm{N}}^{\mathrm{mic}}}$ is the integrity parameter of the normal direction, and $\beta_{\mathrm{T}}^{\mathrm{mic}} = \sqrt{1 - \omega_{\mathrm{T}}^{\mathrm{mic}}}$ is the integrity parameter of the tangential direction.

After homogenizing the microplane state variables, the macroscopic relation between stress and strain tensor is obtained, allowing for the introduction of the constitutive equations in the form of a material subroutine within a finite element (FE) package, enabling further calculations within a spatial discretization, as illustrated in Fig. 2a.

4 LATTICE DISCRETE MODEL

The lattice discrete particle model (LDPM) is employed for an explicit simulation of the mesostructure of concrete [21]. The model represents the material as a system of particles with translational and rotational degrees of freedom. Rigid particles represent larger aggregates with surrounding cement matrix; smaller aggregates are omitted, their role being merged into the constitutive laws on contacts of the larger rigid particles. The kinematics of the model are provided by rigid-body motion of the particles, which results in displacement jumps between them.

Spatial domain discretization: The material inner structure is characterized by Delaunay triangulation, which connects the center of each rigid particle, representing the aggregates, to create the lattice system. Then, a tessellation of the domain generates a network of polyhedral cells, which contain an aggregate surrendered by the cement matrix skeleton. The interaction between aggregates occurs through the facets of the polyhedral cells of adjacent particles.

Kinematics: The displacement $\boldsymbol{u}_p$ of an arbitrary point $\boldsymbol{p}$ within a rigid body can be expressed in terms of the displacements $\boldsymbol{u}_a$ of the particle governing node $\boldsymbol{a}$ and the rotations $\boldsymbol{\theta}_a$ of the rigid body a, as formulated in [13]

$$\boldsymbol{u}_p = \boldsymbol{u}_a + \boldsymbol{\theta}_a \times (\boldsymbol{p} - \boldsymbol{a}) \qquad \begin{Bmatrix} u_1^p \\ u_2^p \\ u_3^p \end{Bmatrix} = \underbrace{\begin{bmatrix} 1 & 0 & 0 & 0 & x_3^p - x_3^a & x_2^a - x_2^p \\ 0 & 1 & 0 & x_3^a - x_3^p & 0 & x_1^p - x_1^a \\ 0 & 0 & 1 & x_2^p - x_2^a & x_1^a - x_1^p & 0 \end{bmatrix}}_{\boldsymbol{A}_a^p} \begin{Bmatrix} u_1^a \\ u_2^a \\ u_3^a \\ \theta_1^a \\ \theta_2^a \\ \theta_3^a \end{Bmatrix} \tag{17}$$

where the subscripts 1, 2, and 3 refer to the three coordinate directions. In this description of rigid body motion, small deformations and rotations are assumed. Consider two rigid bodies, a and b, with one common contact facet, as illustrated in Fig. 2b. Assuming arbitrary displacements and rotations for a and b, the displacement of point c at the contact facet can be expressed by substituting c and a, and c and b into Eq. (17). The difference between the displacements from both sides of each contact facet results in the following expression for the displacement jump between rigid bodies a and b at the centroid of the contact facet, $\boldsymbol{c}$.

$$\Delta \boldsymbol{u}_{ab} = \boldsymbol{A}_b^c (\boldsymbol{u}_b \boldsymbol{\theta}_b)^T - \boldsymbol{A}_a^c (\boldsymbol{u}_a \boldsymbol{\theta}_a)^T \tag{18}$$

Stress-displacement relation: The interaction of particles is governed by constitutive relations that are applied at their contact facets. The mesoscale elastic behavior is controlled by two parameters, namely the elastic modulus in the normal direction E_N and in the tangential direction E_T. The relation between

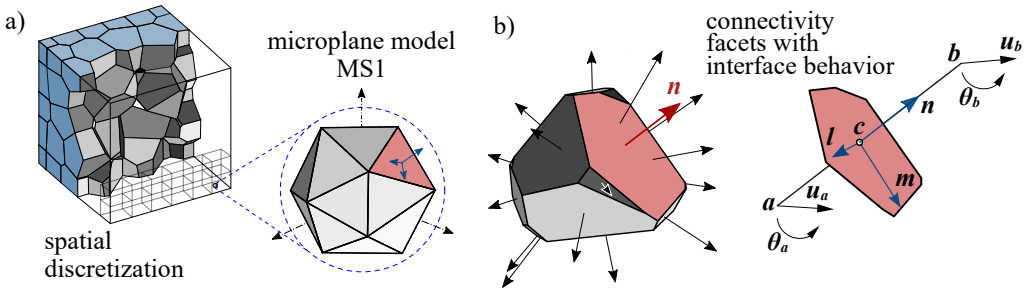

Figure 2: a) cell with connections to neighboring particle centers, b) contact facet between particles associated with nodes $\boldsymbol{a}$ and $\boldsymbol{b}$

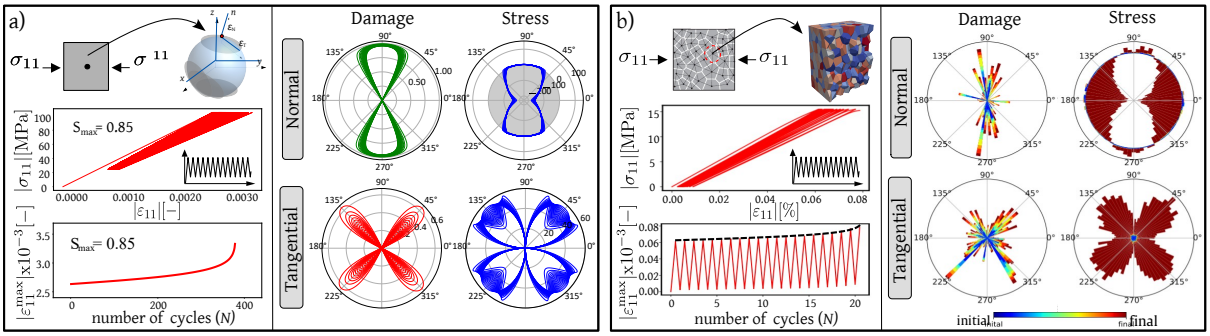

Figure 3: Elementary studies of the 2D microplane model behavior under monotonic and cyclic/fatigue compressive loading showing the stress redistribution at the microplane level. Left: the macroscopic behavior of the single material point. Right: Evolution and distribution of strains, damage, plastic strains and stresses at each microplane

stress σ and displacements $\boldsymbol{u}$ in the elastic regime on each facet yields

$$\begin{Bmatrix} \sigma_N \\ \sigma_M \\ \sigma_L \end{Bmatrix} = \begin{bmatrix} E_\mathrm{N} & & \\ & E_\mathrm{T} & \\ & & E_\mathrm{T} \end{bmatrix} \begin{Bmatrix} u_N \\ u_M \\ u_L \end{Bmatrix} \tag{19}$$

In nonlinear regime, the contact constitutive behavior comes from the relations described in Sec. 2.

Balance equation: The solution of unknown displacements is obtained via enforcing the principle of virtual work. We equilibrate the work of forces (forces $\boldsymbol{f}_a$, $\boldsymbol{f}_b$ and moments $\boldsymbol{m}_a$, $\boldsymbol{m}_b$) acting on virtual nodal displacements ($\delta\boldsymbol{u}_a$, $\delta\boldsymbol{u}_b$ and $\delta\boldsymbol{\theta}_a$, $\delta\boldsymbol{\theta}_b$) with the work of forces ($\boldsymbol{s}$ from Eq. 19 multiplied by the contact area A) acting on facet virtual jumps ($\delta\boldsymbol{\Delta u}_{ab} = L\,\delta\boldsymbol{e}_{ab}$):

$$\begin{pmatrix} \boldsymbol{f}_a & \boldsymbol{m}_a & \boldsymbol{f}_b & \boldsymbol{m}_b \end{pmatrix} \begin{pmatrix} \delta\boldsymbol{u}_a & \delta\boldsymbol{\theta}_a & \delta\boldsymbol{u}_b & \delta\boldsymbol{\theta}_b \end{pmatrix}^T = A\,\boldsymbol{\sigma}^T \delta\boldsymbol{\Delta u}_{ab} \tag{20}$$

5 NUMERICAL EXAMPLES

To fairly compare the macroscale and mesoscale models, both the microplane and lattice discrete particle models apply the same dissipation hypothesis from Sec. 1. This section examines anisotropic damage evolution and triaxial stress redistribution, providing insights into the mechanical deterioration of concrete under uniaxial compressive fatigue. A comparison of the models is made for a cylindrical specimen

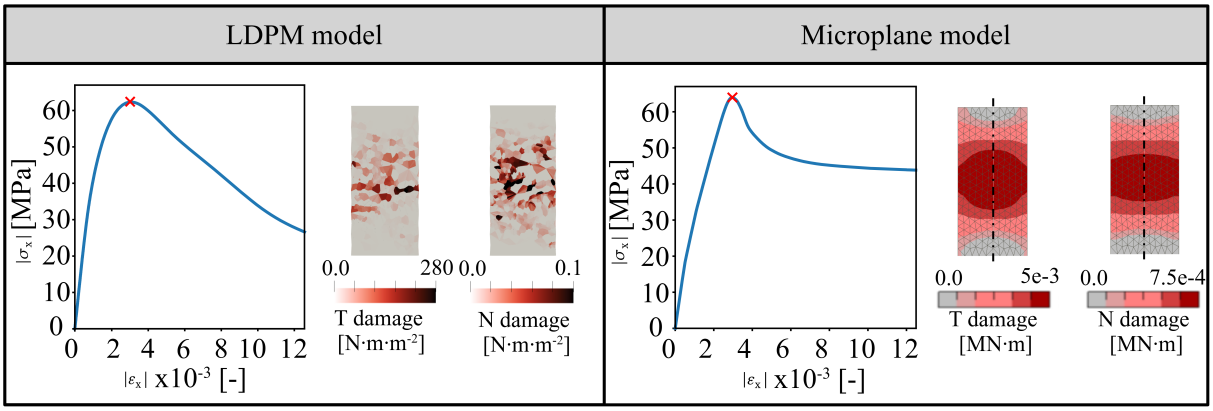

Figure 4: Elementary studies of the 2D microplane model behavior under monotonic and cyclic/fatigue compressive loading showing the stress redistribution at the microplane level. Left: the macroscopic behavior of the single material point. Right: Evolution and distribution of strains, damage, plastic strains and stresses at each microplane

under uniaxial compression, with thermodynamic formulation enabling numerical evaluation of energy dissipation. Contour plots of energy dissipation and a simulation under subcritical cyclic loading are also presented, focusing on hysteretic loop shapes and energy dissipation profiles.

5.1 FATIGUE BEHAVIOR OF A MATERIAL ZONE

Figure 3 presents simulations at a material zone level using the microplane and LDPM models to verify their behavior under subcritical compressive cyclic loading and their ability to represent stress redistribution in an idealized material structure. In Fig. 3a, a simulation of compressive fatigue using the microplane model with loading levels $S_{\max} = 0.85$ and $S_{\min} = 0.20$ is shown. Polar diagrams depict the evolution of damage and stress at each microplane per loading cycle, illustrating the model's realistic reproduction of fatigue-induced anisotropic damage and stress redistribution. Fig. 3b shows a similar study with the LDPM model, where the state variables associated with the normal of each facet are plotted in polar diagrams, with the first and last cycles marked in blue and red, respectively. Both models display similar patterns of normal and tangential damage distribution and corresponding stress profiles, suggesting that the microplane model, despite being a semi-multiscale model, can effectively homogenize stress at the inter-aggregate level for efficient fatigue simulation. However, the microplane model's lack of explicit consideration for concrete's mesostructure limits its ability to capture certain effects, such as damage localization, crack propagation, and aggregate interlock, which the LDPM model inherently accounts for.

5.2 MONOTONIC BEHAVIOR OF A CYLINDER - MICROPLANE AND LDPM

A uniaxial compression cylinder test simulation was conducted using both the LDPM and FE idealization methods. The interface model was integrated at the facet level within the LDPM model and at the microplane level within the FE idealization. To reduce computational time, the FE model utilized an axisymmetric idealization, with lateral constraints applied to the top and bottom of the specimen to induce axisymmetric failure. Correspondingly, the LDPM cylinder model was also laterally constrained at its top and bottom ends. For efficiency, the cylinder dimensions were maintained at a height of 10 cm and a diameter of 5 cm.

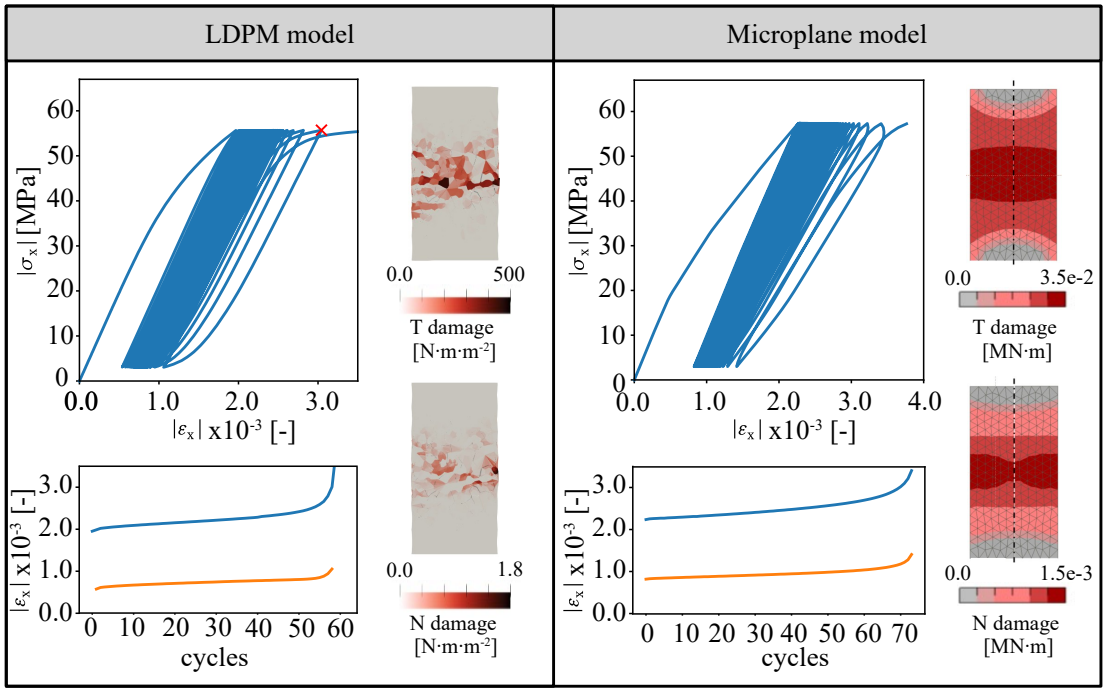

Figure 5: Elementary studies of the 2D microplane model behavior under monotonic and cyclic/fatigue compressive loading showing the stress redistribution at the microplane level. Left: the macroscopic behavior of the single material point. Right: Evolution and distribution of strains, damage, plastic strains and stresses at each microplane

The material parameters of the FE-microplane and LDPM-slide models have been calibrated to yield comparable compressive strength for both models, as shown in the stress-strain diagrams of both the top and bottom panels of Fig. 4. It can be observed that the simulation using LDPM exhibits a more realistic post-peak behavior in comparison to the FE simulation. This discrepancy may be attributed to the selected material parameters. On the other hand, the discrete nature and explicit representation of multiple cracks inherent to LDPM idealization may facilitate the replication of post-peak softening behavior in concrete more effectively than continuum-based approaches.

The bottom row of Fig. 4 display contour plots of energy dissipation due to damage in the normal and tangential direction at the peak load. Dissipation due to damage has been chosen as the displayed state variable based on the results presented in [22, 23, 24], where it was found that energy dissipation due to damage under fatigue loading remains constant for the same stress configuration. The displayed results show a distributed damage pattern for both FE and LDPM simulation on the central zone of the specimen, which is to be expected due to the restrained upper and lower parts. For both simulations the energy dissipation due to tangential damage is clearly larger than the dissipation due to normal damage. As a remark about the values of the dissipation one needs to take into account that the enhery dissipation has been measured in MN · m for the FE results and in N · mm · mm^{-2} for the LDPM simulation.

5.3 FATIGUE BEHAVIOR OF A CYLINDER - MICROPLANE AND LDPM

The behavior of concrete under subcritical cyclic loading, as modeled by both the microplane and LDPM models, is summarized in Fig. 5. The top row displays the stress-strain curves. The hysteretic loops observed indicate that both models effectively reproduce damage accumulation during unloading. This

phenomenon in concrete arises because aggregates attempt to return to their original positions during unloading but are hindered by plastic deformations from the loading phase. The reduction in stiffness observed in the lower part of the hysteretic loop, corroborated by acoustic emission studies showing significant damage accumulation at lower stress levels [25], supports this conclusion. The microplane model MS1 simulates this behavior by allowing some microplanes to enter the inelastic regime in the tangential direction upon unloading. The LDPM model provides an even more realistic simulation by explicitly considering the skeleton of aggregates and cement paste, thus accounting for the rearrangements of aggregates during the loading-unloading cycles. Below each stress-strain curve, a set of creep-fatigue curves is displayed for each respective simulation, showing comparable results that align closely with experimental data.

The bottom row of Fig. 4 displays contour plots of energy dissipation due to damage in the normal and tangential direction at the end of the simulation. The displayed results illustrate a distributed damage pattern for both the FE and LDPM simulations in the central zone of the specimen. For both simulations, the energy dissipation due to tangential damage is greater than the dissipation due to normal damage. These results are consistent with those shown for monotonic loading. However, it is notable that the energy dissipation has increased in comparison to the energy dissipated under monotonic loading up to the peak. This indicates that under subcritical cyclic loading, the damage process is more distributed within the volume of the specimen.

6 CONCLUSIONS

To model the fatigue behavior of concrete under compression, along with the associated stress redistribution and anisotropic damage evolution, we employed the microplane and lattice discrete particle model (LDPM). In order to ensure a fair comparison of the advantages and limitations of macroscale and mesoscale models, both the microplane and LDPM were integrated with the same dissipation hypothesis in their constitutive equations. Simulations at the interface and material point levels yielded realistic results, accurately capturing anisotropic damage evolution and stress redistribution in single material point simulations using the microplane model MS1. When comparing the simulations of a concrete cylinder under monotonic fatigue compressive loading, both models exhibited comparable results, including post-peak behavior and the realistic shape of hysteretic loops during subcritical cyclic loading. The shape of these loops effectively depicted damage accumulation upon unloading, in accordance with experimental observations. Due to the included thermodynamic formulation, it was possible to evaluate the energy dissipation. The results indicated that the dissipation due to tangential damage was greater than that due to normal damage for both monotonic and subcritical cyclic loading. This highlights the role of the inter-aggregate shear behavior of concrete under compression. Overall, both the macros- and mesoscale models demonstrated their capacity to accurately reproduce the fatigue behavior of concrete.

ACKNOWLEDGMENT

The work was supported within the framework of the joint project *Energy dissipation-based approach to stochastic fatigue of concrete considering interacting time and temperature effects* (EnFatiCon), supporting the German partner by the German Research Foundation (DFG), project number 471796896 and the Czech partner (M. Vořechovský) by the Czech Science Foundation, project number GF22-06684K. We gratefully acknowledge ES3inc for providing MARS, which significantly contributed to the completion of this research.

REFERENCES

[1] A. Baktheer, C. Goralski, J. Hegger, R. Chudoba, Stress configuration-based classification of current research on fatigue of reinforced and prestressed concrete, Structural Concrete (2024). doi:10.1002/suco.202300667.

[2] H. Becks, M. Aguilar, A. Baktheer, R. Chudoba, M. Classen, Experimental and numerical investigations on the fatigue behavior of high-strength concrete under combined shear-compression loading, IABSE Proceedings of IABSE symposium: challenges for existing and oncoming structures, Prague, Czech Republic (2022) 532–540.

[3] A. Baktheer, H. Spartali, R. Chudoba, J. Hegger, Concrete splitting and tip-bearing effect in the bond of anchored bars tested under fatigue loading in the push-in mode: An experimental investigation, Materials and Structures 55 (3) (2022) 101. doi:10.1617/s11527-022-01935-7.

[4] A. Alliche, Damage model for fatigue loading of concrete, International Journal of Fatigue 26 (9) (2004) 915–921. doi:10.1016/j.ijfatigue.2004.02.006.

[5] R. Desmorat, F. Ragueneau, H. Pham, Continuum damage mechanics for hysteresis and fatigue of quasi-brittle materials and structures, International Journal for Numerical and Analytical Methods in Geomechanics 31 (2) (2007) 307–329. doi:10.1002/nag.532.

[6] A. Baktheer, E. Martínez-Pañeda, F. Aldakheel, Phase field cohesive zone modeling for fatigue crack propagation in quasi-brittle materials, Computer Methods in Applied Mechanics and Engineering (2024) 116834doi:10.1016/j.cma.2024.116834.

[7] A. Baktheer, R. Chudoba, Classification and evaluation of phenomenological numerical models for concrete fatigue behavior under compression, Construction and Building Materials 221 (2019) 661 – 677. doi:10.1016/j.conbuildmat.2019.06.022.

[8] K. Kirane, Z. P. Bažant, Microplane damage model for fatigue of quasibrittle materials: Sub-critical crack growth, lifetime and residual strength, International Journal of Fatigue 70 (2015) 93–105. doi:10.1016/j.ijfatigue.2014.08.012.

[9] A. Baktheer, M. Aguilar, R. Chudoba, Microplane fatigue model MS1 for plain concrete under compression with damage evolution driven by cumulative inelastic shear strain, International Journal of Plasticity 143 (2021). doi:10.1016/j.ijplas.2021.102950.

[10] V. Cervenka, J. Cervenka, R. Pukl, Atena—a tool for engineering analysis of fracture in concrete, Sadhana 27 (4) (2002) 485–492. doi:10.1007/BF02706996.

[11] I. Boumakis, G. Di Luzio, M. Marcon, J. Vorel, R. Wan-Wendner, Discrete element framework for modeling tertiary creep of concrete in tension and compression, Engineering Fracture Mechanics 200 (2018) 263–282. doi:https://doi.org/10.1016/j.engfracmech.2018.07.006.
URL https://www.sciencedirect.com/science/article/pii/S0013794418302492

[12] A. Cibelli, R. Wan-Wendner, L. Wan-Wendner, J. Vorel, D. Pelessone, MARS–a multiphysics framework for the analysis of cast and printed concrete, DBMC 2023 (2023).

[13] G. Cusatis, D. Pelessone, A. Mencarelli, Lattice discrete particle model (LDPM) for failure behavior of concrete. I: Theory, Cement and Concrete Composites 33 (9) (2011) 881 – 890. doi:10.1016/j.cemconcomp.2011.02.011.

[14] J. Eliáš, J.-L. Le, Modeling of mode-I fatigue crack growth in quasibrittle structures under cyclic compression, Engineering Fracture Mechanics 96 (2012) 26 – 36. doi:10.1016/j.engfracmech.2012.06.019.

[15] J. Eliáš, M. Vořechovský, J. Skoček, Z. P. Bažant, Stochastic discrete meso-scale simulations of concrete fracture: Comparison to experimental data, Engineering Fracture Mechanics 135 (2015) 1–16. doi:10.1016/j.engfracmech.2015.01.004.

[16] R. Chudoba, M. Vořechovský, M. Aguilar, A. Baktheer, Coupled sliding–decohesion–compression model for a consistent description of monotonic and fatigue behavior of material interfaces, Computer Methods in Applied Mechanics and Engineering 398 (2022) 115259. doi:10.1016/j.cma.2022.115259.

[17] A. Baktheer, R. Chudoba, Pressure-sensitive bond fatigue model with damage evolution driven by cumulative slip: Thermodynamic formulation and applications to steel- and frp-concrete bond, International Journal of Fatigue 113 (2018) 277 – 289. doi:10.1016/j.ijfatigue.2018.04.020.

[18] A. Baktheer, M. Aguilar, J. Hegger, R. Chudoba, Microplane damage plastic model for plain concrete subjected to compressive fatigue loading, 10th International Conference on Fracture Mechanics of Concrete and Concrete Structures, FraMCoS-X, 2019. doi:10.21012/FC10.233196.

[19] A. Baktheer, S. Esfandiari, M. Aguilar, H. Becks, M. Classen, R. Chudoba, Fatigue-induced stress redistribution in prestressed concrete beams modeled using the constitutive hypothesis of inter-aggregate degradation, Fatigue & Fracture of Engineering Materials & Structures (2024). doi:10.1111/ffe.14388.

[20] I. Carol, Z. P. Bažant, Damage and plasticity in microplane theory, International Journal of Solids and Structures 34 (29) (1997) 3807–3835. doi:10.1016/S0020-7683(96)00238-7.

[21] J. E. Bolander, J. Eliáš, G. Cusatis, K. Nagai, Discrete mechanical models of concrete fracture, Engineering Fracture Mechanics 257 (2021) 108030. doi:10.1016/j.engfracmech.2021.108030.

[22] M. Aguilar, A. Baktheer, R. Chudoba, Numerical investigation of load sequence effect and energy dissipation in concrete due to compressive fatigue loading using the new microplane fatigue model MS1, Onate, E., Peric, D., Chiumenti, M., de Souza Neto, E., Eds; COMPLAS 2021; Barcelona, Spain, 2021. doi:10.23967/complas.2021.053.

[23] M. Aguilar, A. Baktheer, R. Chudoba, On the energy dissipation in confined concrete subjected to shear cyclic loading, Proceedings in Applied Mathematics and Mechanics 22 (1) (2023) e202200301. doi:10.1002/pamm.202200301.

[24] M. Aguilar, A. Baktheer, H. Becks, M. Classen, R. Chudoba, Fatigue-induced concrete fracture under combined compression and shear studied using standard cylinder and refined punch-through shear test setup, 11th International Conference on Fracture Mechanics of Concrete and Concrete Structures (2023). doi:10.21012/FC11.092350.

[25] N. Oneschkow, T. Scheiden, M. Hüpgen, C. Rozanski, M. Haist, Fatigue-induced damage in high-strength concrete microstructure, Materials 14 (19) (2021). doi:10.3390/ma14195650.